

Active Hyperspectral Imaging Using an Event Camera

Supplementary Material

Bohan Yu^{1,2†} Jinxiu Liang^{1,2} Zhuofeng Wang³
Bin Fan^{1,2} Art Subpa-asa⁴ Boxin Shi^{1,2*} Imari Sato⁴

¹ State Key Laboratory for Multimedia Information Processing, School of Computer Science, Peking University

² National Engineering Research Center of Visual Technology, School of Computer Science, Peking University

³ School of Electronics Engineering and Computer Science, Peking University ⁴ National Institute of Informatics

ybh1998@pku.edu.cn, cssherryliang@pku.edu.cn, wangzf2003@stu.pku.edu.cn,

binfan@pku.edu.cn, subpa@nii.ac.jp, shiboxin@pku.edu.cn, imarik@nii.ac.jp

6. More Implementation Details

6.1. More Details on Calibration

Constant light intensity calibration. We employ a smart-phone display as a constant light source to provide stable baseline illumination. The absolute intensity c is measured using a calibrated radiometer. While this parameter is crucial for absolute intensity measurements, it can be adjusted arbitrarily when only relative spectral information is required, effectively serving as an exposure control parameter.

Spectral response calibration. We employ an end-to-end calibration approach for the camera’s spectral response $D(\lambda)$ using a color checker’s white region as a reference. By comparing our system’s reconstruction against ground truth measurements from a spectrometer, we derive channel-specific correction factors that compensate for both the camera’s spectral sensitivity and other systematic non-idealities in the imaging pipeline.

Event threshold calibration. The event triggering threshold C is calibrated using the color checker’s grayscale patches, utilizing their known linear intensity relationship. We perform an end-to-end calibration by adjusting the threshold value until the reconstructed intensities of the gray patches exhibit the expected linear distribution. This approach simultaneously accounts for positive and negative contrast thresholds, assuming symmetric triggering behavior.

Co-axial setup of the event camera and illumination. We place the event camera straight below the light source. This horizontal co-axial alignment ensures consistent temporal-spectral mapping, unaffected by object depth. The right picture shows that there is no horizontal cast shadow on the left or right of the rod in the front, and the rainbow is

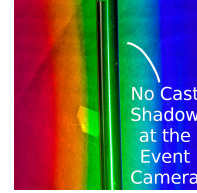


Figure 9. Co-axial setup of the event camera and illumination. The vertical rod does not cast a shadow on the background plate, indicating that the illumination and camera are placed in a horizontally co-axial.

consistent across depth changes. Vertical misalignment may cause shadows in the up and down direction, but does not affect the illumination pattern mapping accuracy. Robustness is also validated through consistent results across the video.

6.2. More Details on Hardware Configuration

As shown in Fig. 2, we employ multiple optical components to construct the “sweeping rainbow” illumination pattern. The physical device is shown in Fig. 10. The working principles of each component in our hyperspectral imaging system are as follows (in light path order):

- **Point light source: Initial illumination.** A xenon arc lamp (Asahi Spectra MAX-303) provides wide, flat spectrum distribution across the visible range, ensuring complete spectral sampling. Its high-intensity output enables reliable event triggering in the camera. The continuous nature of its spectrum is essential for capturing the full range of spectral information without gaps.
- **First convex lens: Concentration.** The first convex lens with a 50mm focal concentrates the light onto a controllable-width slit to maximize light efficiency, a critical factor given the system’s need for sufficient intensity to trigger events.
- **Vertical slit: Width control.** The vertical slit with con-

*Corresponding author: Boxin Shi

†This work was conducted while the first author, Bohan Yu, was doing internship at National Institute of Informatics.

trollable width controls the spatial width of the light beam, which directly influences the final spectrum’s FWHM.

- **Second convex lens: Collimation.** The second convex lens with a 50mm focal transforms the divergent light into parallel rays. This collimation is essential for optimal interaction with the blazed grating, as parallel light ensures consistent diffraction angles across the beam width.
- **Cylindrical convex lens: Shape control.** The cylindrical convex lens with 150mm focal converges the light vertically at the spinning mirror to minimize the required mirror size and then allows the light to diverge vertically, creating the characteristic tall rainbow strip pattern. It optimizes beam shape for efficient scanning.
- **Blazed grating: Spectral separation.** The blazed grating with 600 lines/mm is used for spectral separation. This precise spacing is optimized for visible light diffraction, horizontally dispersing different wavelengths while maintaining high diffraction efficiency. The grating reflects this spectrally separated light toward the mirror array.
- **Rotated mirror array: Temporal scanning.** The four-mirror array driven by a stepper motor and gear system reflects the rainbow strip pattern and sweeps it across the scene in a horizontal pattern. The system achieves rotation speeds up to 1800 revolutions per minute (rpm), enabling rapid spectral scanning while maintaining sufficient dwell time for event generation at each wavelength.

All optical elements are mounted on a vibration-isolated optical breadboard. These components create a precise and efficient spectral scanning system. As to the positions of optical components, 4 of 5 DoFs are fixed for light passing straight through the center. The distances between them are then tuned for maximum brightness at the slit (first lens), narrow output rainbow spectra (second lens), and appropriate 1st-order diffraction within the mirror range (grating). The small diffraction area of the grating ($< 2\text{cm}$) allows approximating light as a point source at the grating’s image in the mirror. Each element’s parameters have been optimized to balance competing requirements: spectral resolution, light efficiency, scanning speed, and system compactness. The result is a system capable of real-time hyperspectral imaging while maintaining the bandwidth efficiency inherent to event-based sensing.

6.3. More Details on Algorithm Configuration

The computational pipeline of the proposed method is built on a hybrid architecture that leverages both CPU and GPU resources. Event pre-processing is accelerated using Numba just-in-time compilation, while the reconstruction algorithms are implemented in PyTorch to utilize GPU parallelization. The experiments are conducted on a single NVIDIA GeForce RTX 3060 graphics card. It takes about 20 seconds to reconstruct a hyper-spectral frame. For visualization purposes, we employ a color space conversion pipeline that transforms

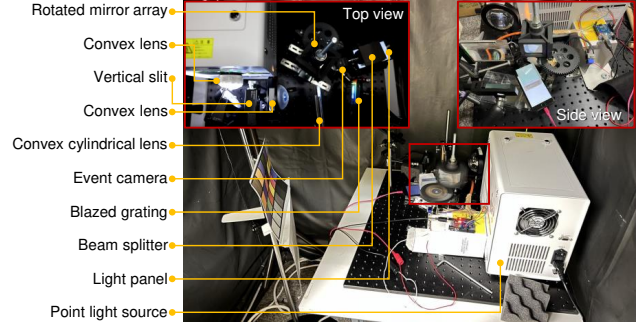


Figure 10. System prototype (corresponding to Fig. 1(a)).

the reconstructed hyperspectral data through CIE 1931 color space before final conversion to RGB using OpenCV’s color management system.

6.4. More Details on Data simulation

Our synthetic dataset generation pipeline simulates the complete optical and sensing characteristics of the system, including the non-ideal narrow-band illumination pattern, non-ideal event triggering, and frame camera imaging noises. The sweeping rainbow effect is modeled using narrow-band illumination with a FWHM of 17.5 nm, convolved with ground truth hyperspectral images to generate 1200 intensity frames. To achieve realistic event generation, we maintain a baseline illumination at 3% of the maximum scene intensity. The event camera’s behavior is carefully modeled with triggering thresholds C following a normal distribution with mean 0.15 and standard deviation 0.01 and incorporating a 50 μs refractory period at a simulated scanning speed of 1800 rpm. During reconstruction, we employ consistent parameter settings with regularization weight $\alpha_{\text{int}} = 1.0$ and M_{start} of $0.3 \times M$. For the frame-based camera, we designed equivalent capture scenarios that match our system’s operating conditions. The frame-based synthetic data incorporates multiplicative white Gaussian noise with a standard deviation of 0.067 to match the noise characteristics of event cameras.

6.5. More Details on Compared methods

We evaluate the proposed system against the following baselines:

- **Full-bandwidth frame-based method.** The frame-based variant with full bandwidth is used for reference, which involves 1200 intensity frames with maximum temporal resolution and highest data bandwidth. Note that, for real-time capture, a high-speed camera over 3,000 FPS is required for the real scenes.
- **Bandwidth-matched frame-based method.** To ensure fair bandwidth comparisons, we account for the 16-bit event data format (assuming that the input event streams employ 16-bit Prophesee EVT 3.0 format) versus 8-bit

grayscale frames, allowing us to determine equivalent frame counts for matched-bandwidth scenarios. The reduced-bandwidth comparisons employ uniformly down-sampled frame sequences with linear interpolation for spectral reconstruction.

- **Parkkinen basis method [38].** To evaluate against basis-based methods, we implemented the Parkkinen basis [38] approach as a representative state-of-the-art technique. Ground truth hyperspectral data is first decomposed using least-squares fitting to the Parkkinen basis functions, followed by reconstruction for comparison with our method. This offers insights into the advantages of our approach for capturing narrow-band spectral features, which is difficult to achieve with basis-based methods.
- **CASSI-based method [25, 58].** To evaluate against CASSI-based methods, we simulate CASSI optical system and evaluate on two state-of-the-art techniques [25, 58].

7. More Analysis

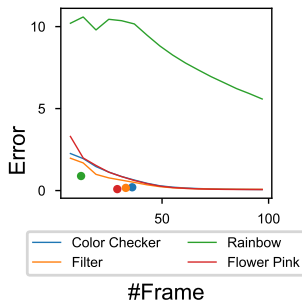


Figure 11. Comparison between frame-based method using different numbers of frames (curves) and ours (solid points) for different samples.

7.1. Bandwidth efficiency

Fig. 11 presents a comprehensive comparison of reconstruction accuracy versus data bandwidth across different methods. Our event-based approach consistently achieves superior spectral reconstruction quality compared to frame-based methods operating at equivalent bandwidth levels. Notably, our method requires only 40.47% of the bandwidth of traditional frame-based approaches to achieve comparable accuracy.

7.2. System parameters

Our detailed analysis of the relationship between planar constant light source intensity, event camera triggering threshold, and data rates reveals important system characteristics. Using a standard 24-patch color checker as our test target, we conducted comprehensive measurements across varying operating conditions. The results in Fig. 12 show that lower

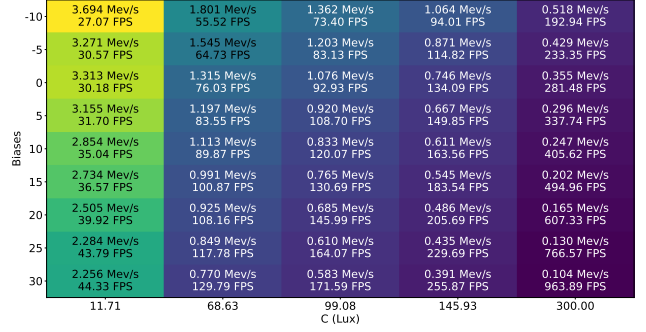


Figure 12. The analysis demonstrates the relationship between light source intensity, event camera bias settings (threshold), and data rates, thereby illustrating how system parameters can be optimized for different operating conditions and bandwidth requirements.

constant light intensities result in higher bandwidth per revolution. For the event triggering threshold, a lower threshold results in higher bandwidth per revolution. Because the Prophesee EVK4 IMX636 event camera we are using has 80 Mev/s maximum event triggering, we also calculate the theoretical maximum FPS for each setup. The final maximum FPS is also limited by the mechanical maximum rotation speed, which is 30 FPS for our current device.

Ours	DESCI [25]	GAPTV [58]
6.65	5.80	7.30

Table 1. Comparison with CASSI-based methods. Quantitative results with real and fake flowers.

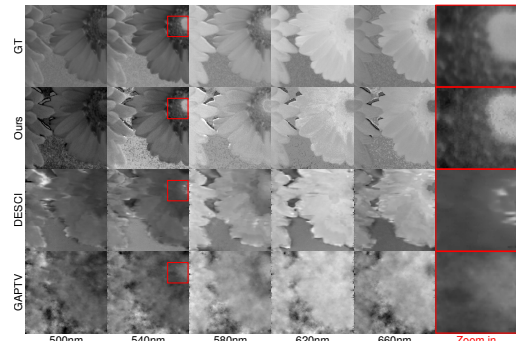


Figure 13. Comparison with CASSI-based methods. Qualitative results with real and fake flowers.

7.3. Comparison with CASSI-based methods

CASSI methods often exhibit horizontal artifacts due to the spectral-spatial encoding. Comparisons with representative CASSI methods DESCI [25] and GAPTV [58] are shown in Figure 13, with their SAM scores in Table 1. Our method leverages high temporal resolution and low bandwidth properties of event cameras and constructs spectral-temporal

encoding, avoiding cross-pixel artifacts.

8. More Results

We provide comprehensive hyperspectral reconstruction results that extend beyond the examples presented in the main text. The wavelength labels of the narrow-band images, like ‘380nm’, indicate the beginning of the spectral range.

Comparison results. In Fig. 5 of the main text, we evaluate our method’s capability to recover high-frequency spectral features of the vertical rainbow produced by the prism, comparing with ground truth, basis-based method, bandwidth-matched frame-based method. The corresponding full hyperspectral reconstruction results of different methods are shown in Fig. 14.

Results on static scenes. We include additional four examples on static scenes in Figs. 16 to 19, which contains hyperspectral reconstruction results on white daisies, yellow daisies, pink roses, and yellow roses, respectively. These examples highlight our system’s ability to distinguish between subtle spectral signatures that appear identical to the human eye.

Results on dynamic scenes. For dynamic scenes, we present the full hyperspectral reconstruction results of the iridescent sticker paper under varying viewing angles in Fig. 20 corresponding to Fig. 8 in the main text. We also present additional two new examples in Figs. 21 and 22, which show results on a deforming colorful soft toy under manual manipulation, and a compact disc exhibiting varying spectral responses across its reflection strip, respectively.

Video results. We also provide a supplementary video to demonstrate the complete workflow of our system, from hardware setup to real-time reconstruction. It includes detailed visualization of the “sweeping rainbow” effect, event generation patterns, and reconstruction results. The video also shows real-time visualizations of our three dynamic scenes shown in Figs. 20 to 22, effectively illustrating the system’s capability to capture rapid spectral variations. The video also serves to validate our claims regarding temporal resolution and system responsiveness under real-world conditions.



Figure 14. The full hyperspectral reconstruction results for examples in Fig. 5. Comparative analysis of spectral reconstruction on a high-frequency rainbow pattern. Compared methods include (a) ground truth, (b) ours, (c) basis-based method, and (d) bandwidth-matched frame-based method.

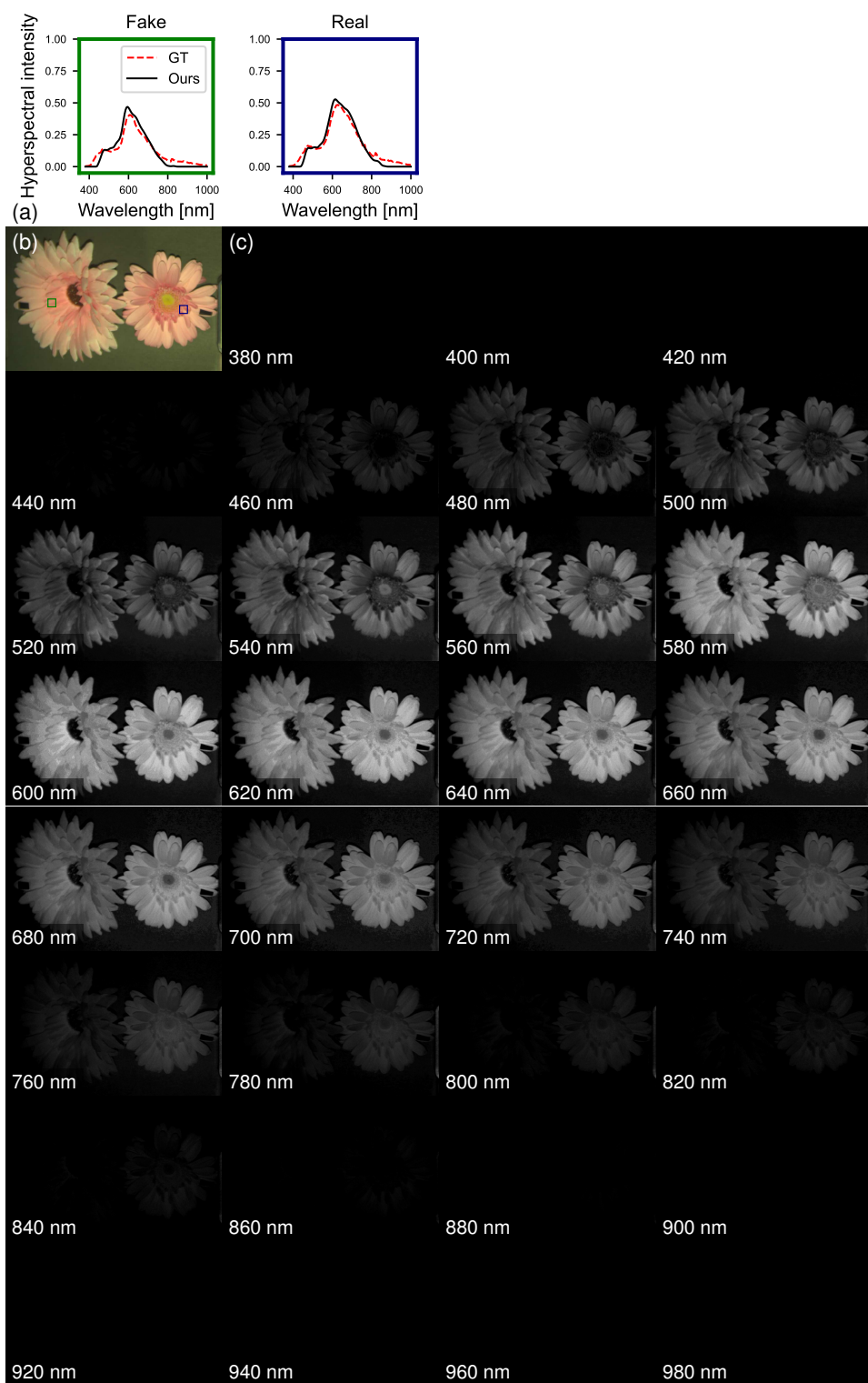


Figure 15. The full hyperspectral reconstruction results for samples in Fig. 7. (a) Spectra of metameric samples against ground truth measurements, highlighting the system’s ability to capture subtle spectral differences. (b) The reconstructed hyperspectral image in sRGB. (c) Estimated hyperspectral images.



Figure 16. Evaluation of metamerism of real (left) and fake (right) white daisies. (a) Spectra of metamerism samples against ground truth measurements, highlighting the system’s ability to capture subtle spectral differences. (b) The reconstructed hyperspectral image in sRGB. (c) Estimated hyperspectral images.

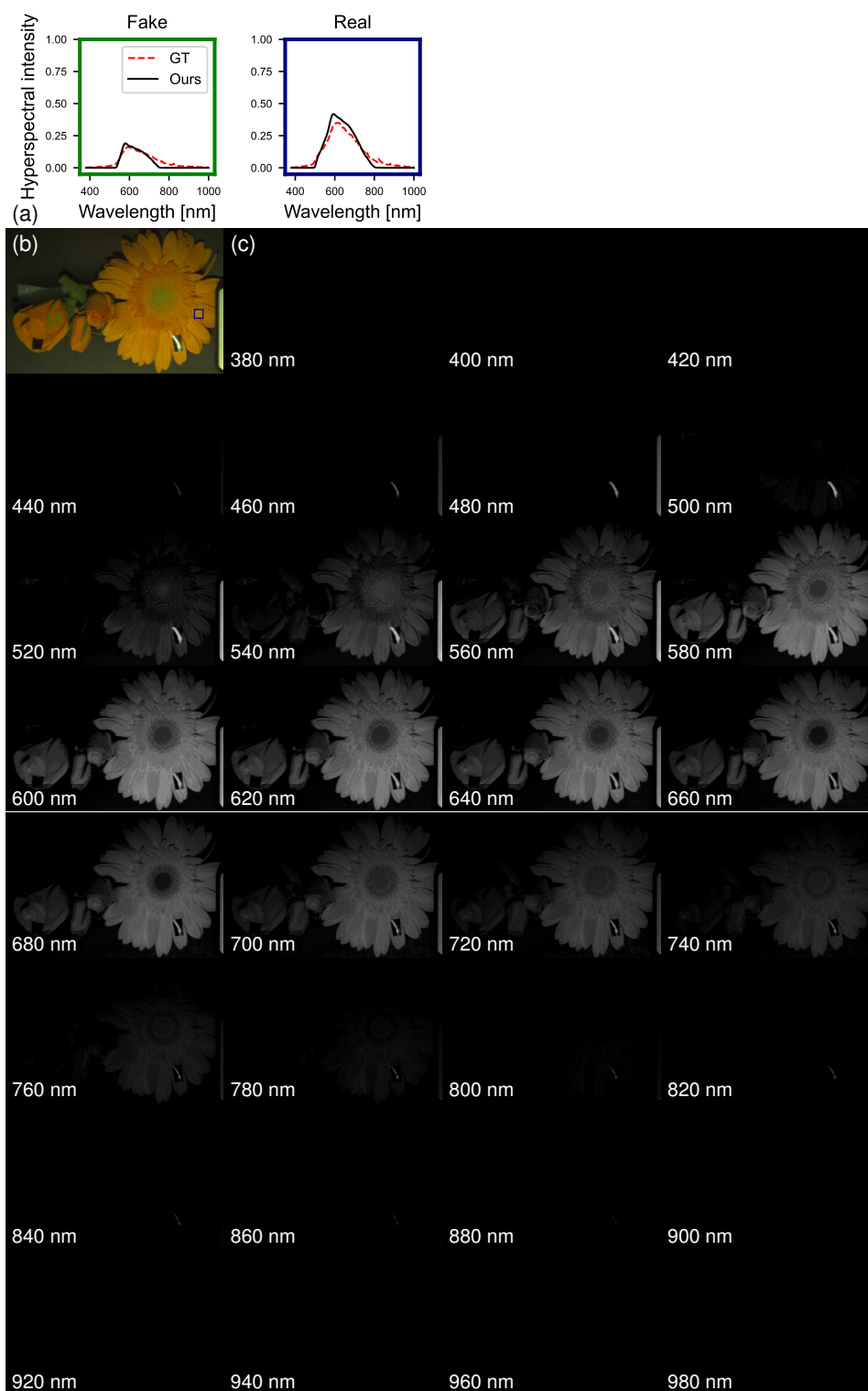


Figure 17. Evaluation of metameric samples of yellow rose (left) and daisy (right). (a) Spectra of metameric samples against ground truth measurements, highlighting the system's ability to capture subtle spectral differences. (b) The reconstructed hyperspectral image in sRGB. (c) Estimated hyperspectral images.

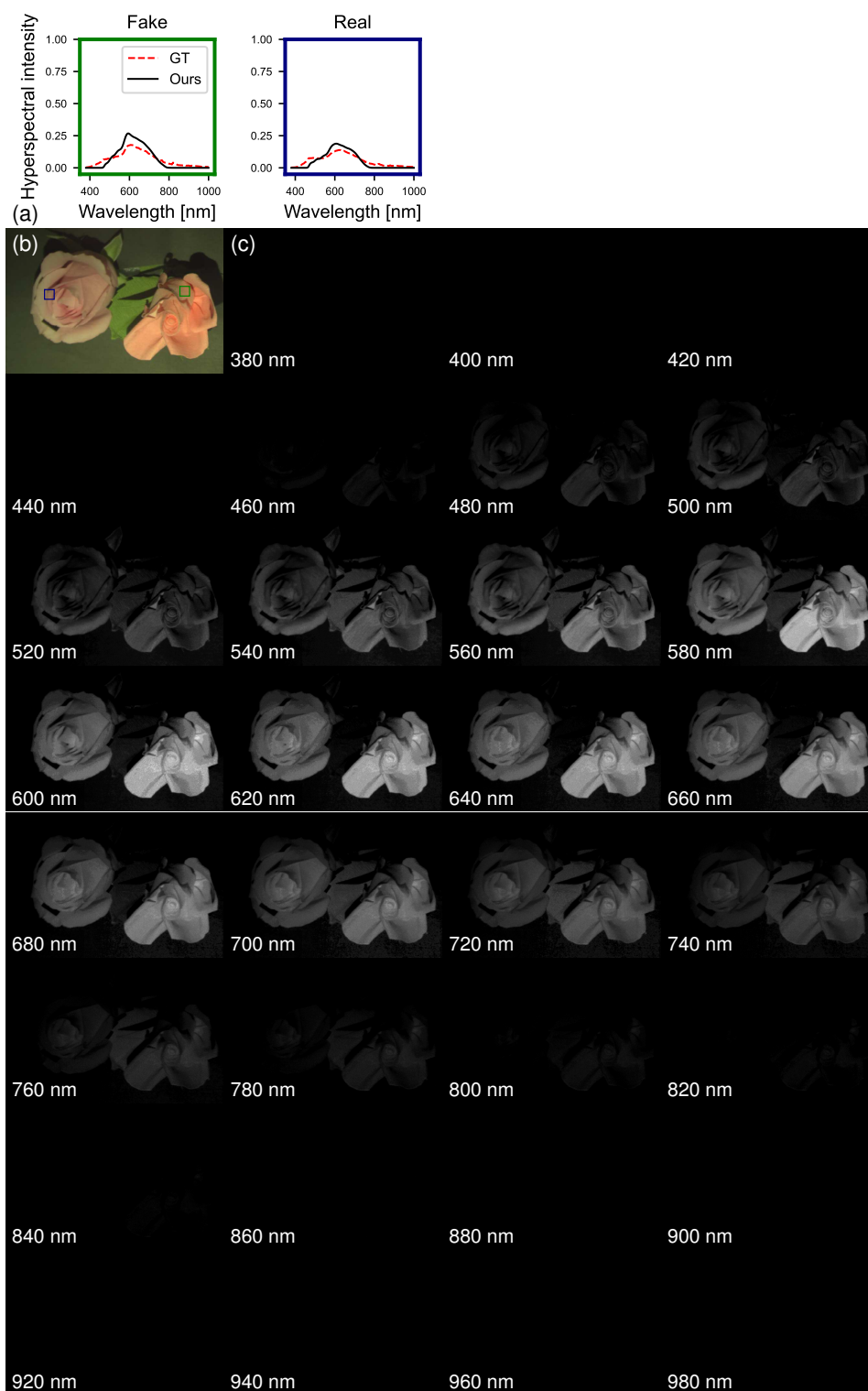


Figure 18. Evaluation of metameric samples of real (left) and fake (right) pink roses. (a) Spectra of metameric samples against ground truth measurements, highlighting the system's ability to capture subtle spectral differences. (b) The reconstructed hyperspectral image in sRGB. (c) Estimated hyperspectral images.

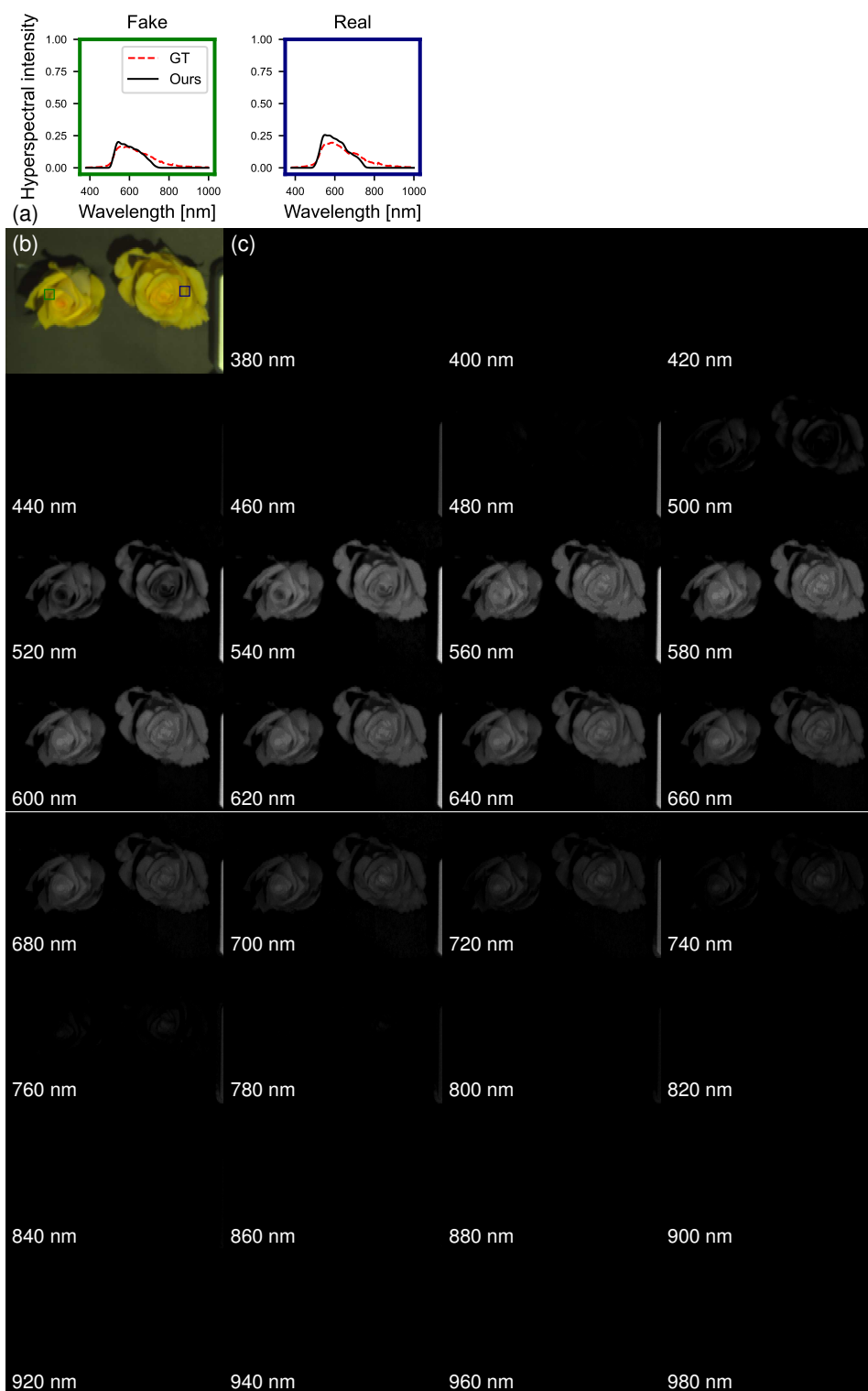


Figure 19. Evaluation of metamer samples of fake (left) and real (right) yellow roses. (a) Spectra of metamer samples against ground truth measurements, highlighting the system's ability to capture subtle spectral differences. (b) The reconstructed hyperspectral image in sRGB. (c) Estimated hyperspectral images.

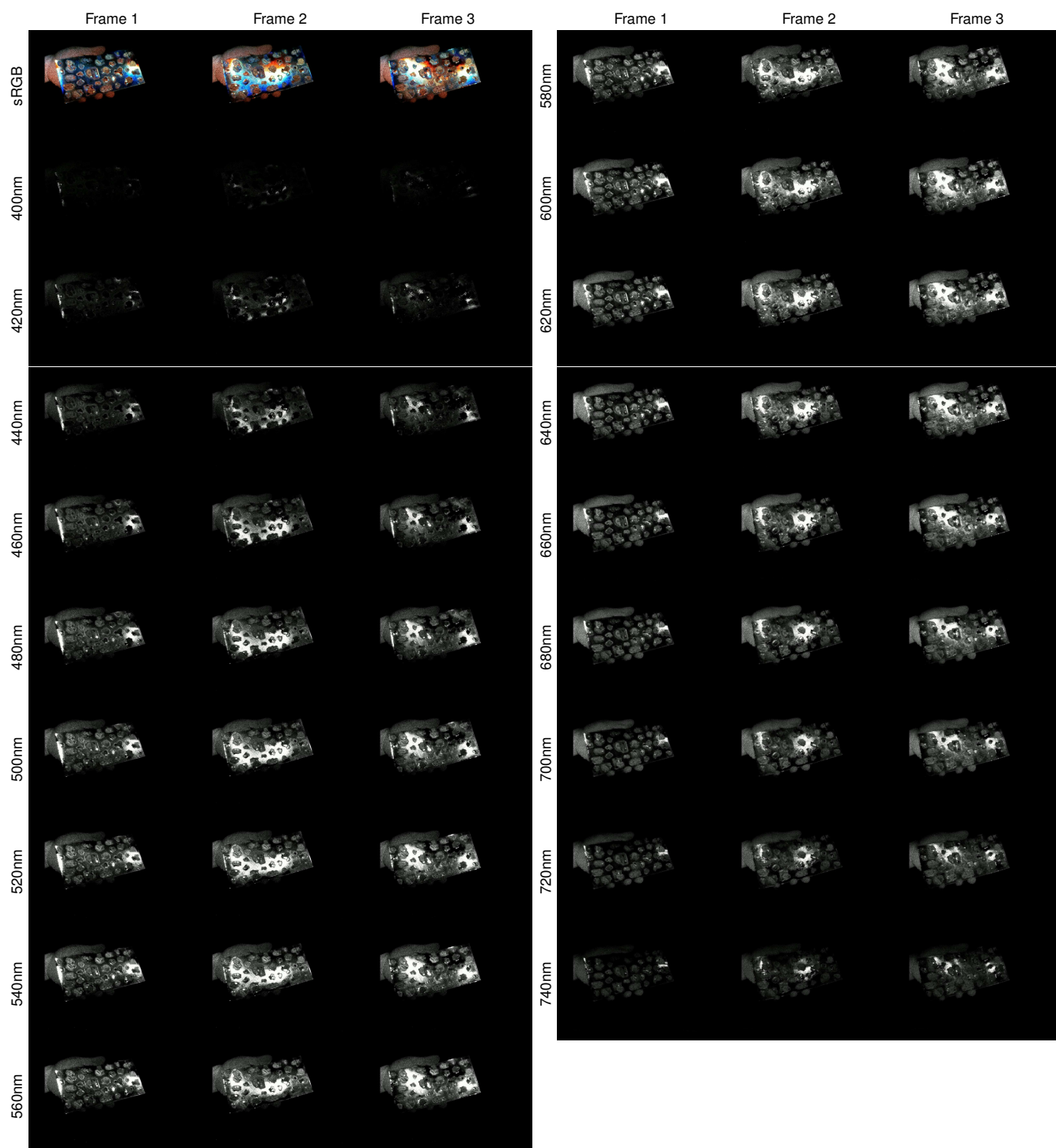


Figure 20. Real-time hyperspectral imaging on a moving iridescent sticker paper. Top-left: Three consecutive estimated hyperspectral images rendered in sRGB. Remaining panels: Corresponding estimated hyperspectral images (380-780nm, sampled at 20nm intervals).

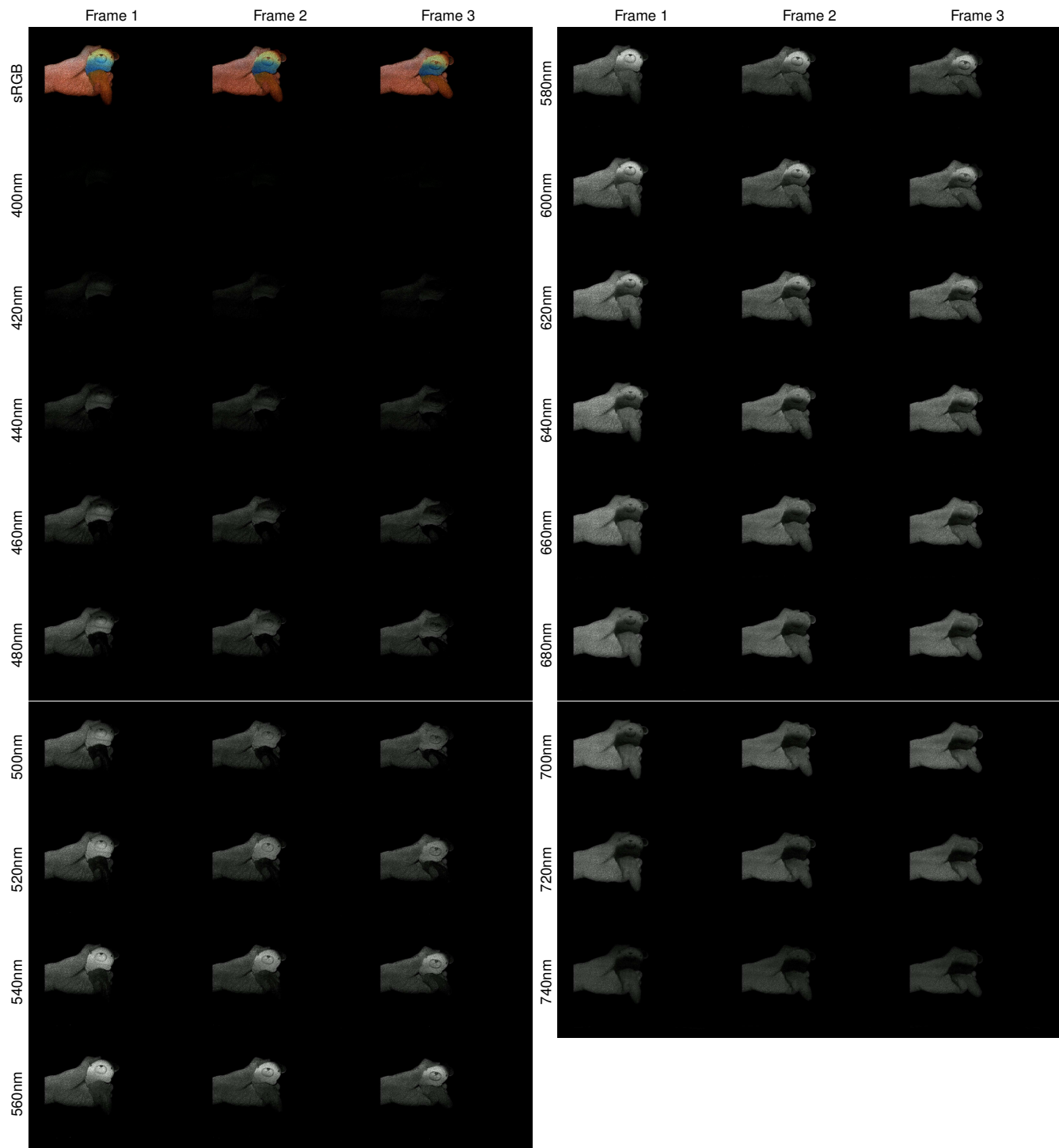


Figure 21. Real-time hyperspectral imaging on a deforming colorful soft toy under manual manipulation. Top-left: Three consecutive estimated hyperspectral images rendered in sRGB. Remaining panels: Corresponding estimated hyperspectral images (380-780nm, sampled at 20nm intervals).

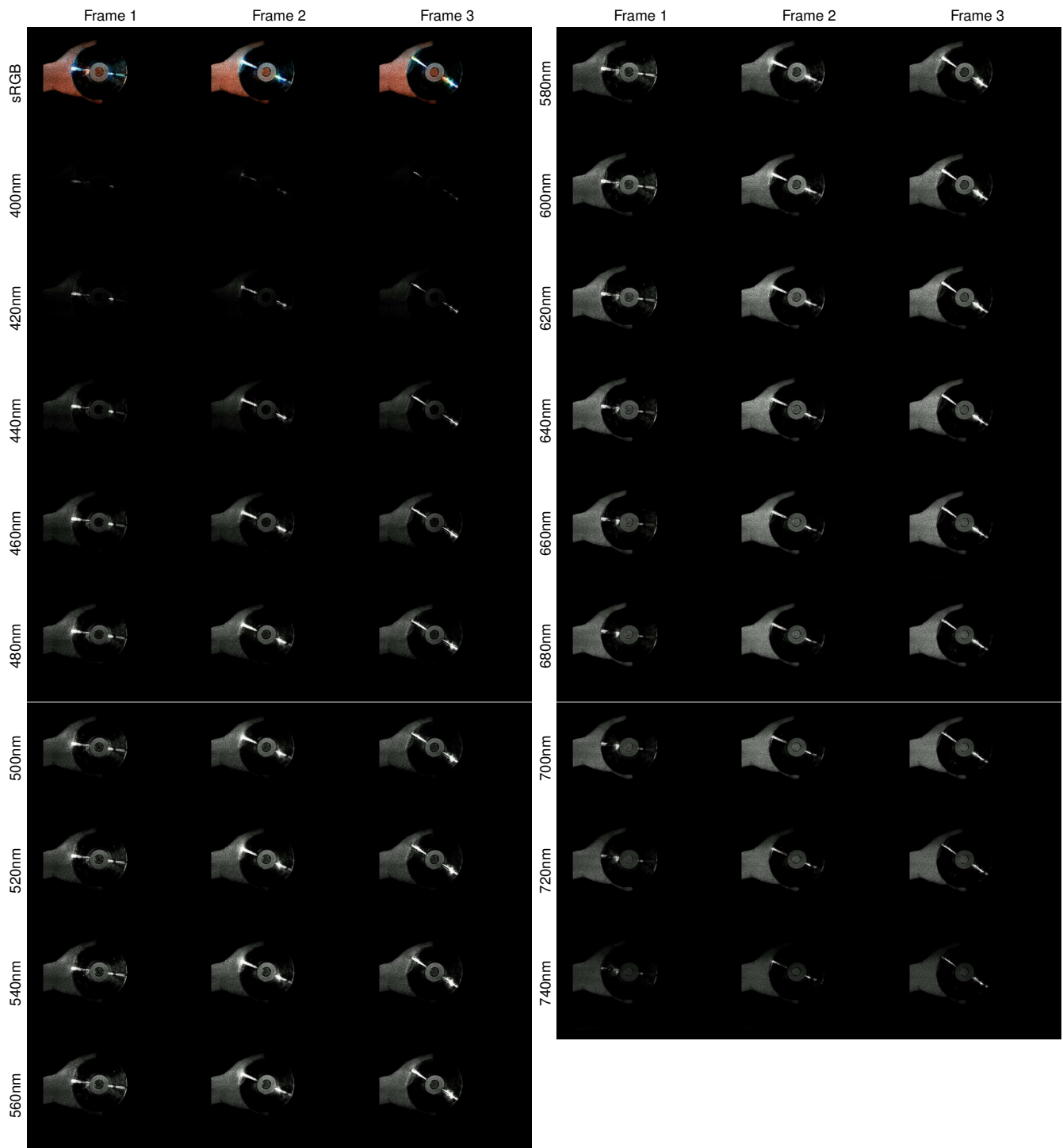


Figure 22. Real-time hyperspectral imaging on a compact disc exhibiting varying spectral responses across its reflection strip. Top-left: Three consecutive estimated hyperspectral images rendered in sRGB. Remaining panels: Corresponding estimated hyperspectral images (380-780nm, sampled at 20nm intervals).